

Journal of Biomedical Optics

SPIEDigitalLibrary.org/jbo

Monitoring the process of pulmonary melanoma metastasis using large area and label-free nonlinear optical microscopy

Daozhu Hua
Shuhong Qi
Hui Li
Zhihong Zhang
Ling Fu

Monitoring the process of pulmonary melanoma metastasis using large area and label-free nonlinear optical microscopy

Daozhu Hua,^{a,b} Shuhong Qi,^{a,b} Hui Li,^{a,b} Zhihong Zhang,^{a,b} and Ling Fu^{a,b}

^aHuazhong University of Science and Technology, Britton Chance Center for Biomedical Photonics, Wuhan National Laboratory for Optoelectronics, Wuhan 430074, China

^bHuazhong University of Science and Technology, Key Laboratory of Biomedical Photonics of Ministry of Education, Wuhan 430074, China

Abstract. We performed large area nonlinear optical microscopy (NOM) for label-free monitoring of the process of pulmonary melanoma metastasis *ex vivo* with subcellular resolution in C57BL/6 mice. Multiphoton autofluorescence (MAF) and second harmonic generation (SHG) images of lung tissue are obtained in a volume of $\sim 2.2 \text{ mm} \times 2.2 \text{ mm} \times 30 \mu\text{m}$. Qualitative differences in morphologic features and quantitative measurement of pathological lung tissues at different time points are characterized. We find that combined with morphological features, the quantitative parameters, such as the intensity ratio of MAF and SHG between pathological tissue and normal tissue and the MAF to SHG index versus depth clearly shows the tissue physiological changes during the process of pulmonary melanoma metastasis. Our results demonstrate that large area NOM succeeds in monitoring the process of pulmonary melanoma metastasis, which can provide a powerful tool for the research in tumor pathophysiology and therapy evaluation. © 2012 Society of Photo-Optical Instrumentation Engineers (SPIE). [DOI: 10.1117/1.JBO.17.6.066002]

Keywords: nonlinear optical microscopy; multiphoton autofluorescence; second harmonic generation; pulmonary melanoma metastasis.

Paper 11716 received Dec. 5, 2011; revised manuscript received Apr. 10, 2012; accepted for publication Apr. 19, 2012; published online Jun. 5, 2012.

1 Introduction

The incidence of malignant melanoma has been increasing rapidly worldwide in the last few decades.¹ Despite significant improvements in diagnosis, surgical techniques, general patient care, and local and systemic adjuvant therapies, the most fearsome aspect of cancer is that most deaths are due to metastasis.^{2,3} Currently, the model of pulmonary melanoma metastasis in C57BL/6 mice has been used more and more to study the process of metastasis and to screen novel anti-metastatic drugs as this cancer can be examined over a relatively short period.⁴⁻⁷ However, the biological heterogeneity of cancer cells in the primary neoplasm and metastases and the modification response of a metastatic tumor cell to systemic therapy in the specific organ microenvironment are the main barriers to the treatment of metastases. This reveals that understanding the process of metastasis on the systemic, cellular and molecular levels are the pressing goals of cancer research.^{2,8-10}

Many methods, such as biochemical,^{11,12} cell biology^{13,14} and statistical macroscopy,^{7,15} are classified according to different monitored objectives and have been employed to inspect the physiological changes of pulmonary melanoma metastasis for studying the process of metastasis and evaluating the drug effects. However, these methods can't provide high spatial resolution of the pulmonary tissue. Histological examination is the gold standard for cancer diagnosis as it can reveal tissue and cellular morphologic features with submicron spatial resolution to identify the pathologic stages of the cancer tissue.

Nonetheless, the procedure of histological biopsy is both invasive and time-consuming as it requires hematoxylin and eosin (HE) stain and physical sectioning. Therefore, new techniques that not only provide high spatial resolution but also monitor the physiological changes of pulmonary melanoma metastasis without complicated sample processing are urgently needed.

Nonlinear optical microscopy (NOM) based on multiphoton absorption and second harmonic generation (SHG) has been widely employed to study the structure and function of cells and tissues due to its unique features of submicron resolution, greater penetration depth, low photo-damage and inherent optical sectioning ability.¹⁶ In particular, NOM can provide the visualization of cellular and subcellular structures using plentiful intrinsic chromophores without any pretreatment for the tissue.¹⁷ Intracellular nicotinamide adenine dinucleotide (NADH), triphosphopyridine nucleotide (NADPH) and flavin adenine dinucleotide (FAD) can take part in cellular energy metabolism and induce multiphoton autofluorescence (MAF), shedding light on associated carcinogenesis.^{18,19} In addition, SHG signals arising from collagen fibers can reveal the remodeling of the extracellular matrix (ECM) in the tissue.^{20,21} SHG imaging can evaluate strategies for altering the aging, atherosclerosis and tumor effectively.²²⁻²⁴ In a recent study, it has been demonstrated that the diagnosis based on the morphologic features obtained by NOM agreed with histological examination for 88.6% of the specimens.²⁵

Unfortunately, to the best of our knowledge, NOM has not been employed in the research of pulmonary melanoma metastasis to monitor the physiological changes of pulmonary tissue during the whole process of colonization, which is the one of

Address all correspondence to: Ling Fu, Huazhong University of Science and Technology, Britton Chance Center for Biomedical Photonics, Wuhan National Laboratory for Optoelectronics, Wuhan 430074, China. Tel: +86 02787792033; Fax: +86 02787792034; E-mail: lfu@mail.hust.edu.cn.

two important steps of metastasis.⁸ In addition, although qualitative differences in morphologic features and quantitative measurement of the MAF and SHG tissue images are feasible enough to evaluate the pathologic stages of the cancer tissue,²⁶⁻²⁸ special challenges remain for NOM to study the process of pulmonary melanoma metastasis. First, the diameter of intact pulmonary metastasis melanoma nodules in C57BL/6 mice is usually several millimeters in size in the middle and late stages. Conventional NOM cannot provide morphologic features of such a large region with high resolution due to the limited field of view of hundreds of square microns. Second, accuracy of the quantitative analysis of the tissue is important to evaluate the pathological states. However, it requires large area imaging rather than imaging of a small portion of the tumor tissue.

We report here on monitoring the process of pulmonary melanoma metastasis *ex vivo* using a home-built large area nonlinear optical microscope (LA-NOM) and intrinsic fluorophores in C57BL/6 mice. Lung tissue at different time points after a tail vein injection of cancer cells are characterized by MAF and SHG imaging in a volume of $\sim 2.2 \text{ mm} \times 2.2 \text{ mm} \times 30 \text{ }\mu\text{m}$. Combined with the morphological analysis of MAF and SHG images, quantitative analysis by the MAF and SHG intensity ratio (MAFIR and SHGIR) between pathological tissue and normal tissue, and the MAF to SHG index (MAFSI) are employed to evaluate physiological changes of pulmonary melanoma metastasis. Our results demonstrate that LA-NOM succeeds in evaluating the pathological changes of pulmonary melanoma metastasis in C57BL/6 mice.

2 Materials and Methods

2.1 Sample Preparation

The cell line was grown in tissue culture media (RPMI 1640, Gibco, USA) supplemented with heat-inactivated 10% fetal bovine serum (HyClone, Australian), 100 U/ml penicillin (Gibco, USA), 0.1 mg/ml streptomycin (Gibco, USA) in a humidified atmosphere of 5% CO₂ and 95% air at 37°C. Cells were harvested by trypsin/ethylene diamine tetraacetic acid (EDTA) and washed with serum-free RPMI 1640 medium three times. Cell pellets were resuspended in ice-cold phosphate buffered saline (PBS) with 5×10^5 cells per 0.5 ml.

Female C57BL/6, 6- to 8-week-old mice from Slac Laboratory Animal (Shanghai, China) were used for this research work. The mice were kept under pathogen-free conditions at a constant temperature of 24°C to 26°C and humidity of 30% to 50%, and allowed food and water *ad libitum*. All animal experiments were approved by the Animal Experimentation Ethics Committee of Huazhong University of Science and Technology.

A PBS of 0.5 ml containing 5×10^5 B16 cells was injected into C57BL/6 syngeneic mice intravenously. The mice were sacrificed and the lungs excised at different time points on days 3, 5, 7, 10, 12, 15, 18, 20, and 25 after tail vein injections. Two mice were sacrificed at each time point and a total of 20 mice (2 normal mice and 18 mice injected B16 cells) were imaged. In each mouse, two specimens were taken from the fresh lung tissue after removing excess blood. One specimen was placed into PBS waiting for nonlinear optical imaging. The other specimen was fixed in 4% paraformaldehyde for HE stain and histological examination. Before the appearance of nodules, the specimens were randomly chosen from the fresh tissue. After the nodules

appeared, the specimens were excised from the regions including as many nodules as possible.

2.2 Imaging Instrumentation and Protocol

Combined MAF and SHG imaging was performed on the home-built LA-NOM in this study, as shown in Fig. 1. Ti:Sapphire laser (Maitai BB, Spectra-Physics) was used as the excitation source (pulse duration: ~ 100 fs, repetition rate: 80 MHz and tunable range: 710 to 980 nm). The excitation beam was scanned by two perpendicular galvanometer mirrors (Model 6215, Cambridge Technology). Serial images were obtained by translating the specimen using a sample translation stage (ES111, Prior Scientific) after each optical scanning imaging and combined into a large area imaging section. Axial scanning was achieved by a piezoelectric stage (P-563.3CD, Physik Instrumente). After splitting from the excitation laser by a long wave pass dichroic mirror (FF665, Semrock) and through a short wave pass emission filter (FF680/SP, Semrock), the auto-fluorescence and SHG signals were separated into two simultaneous detection channels by a dichroic mirror (FF409, Semrock). Two filters (380/14 nm and 485/70 nm, Semrock) and PMTs (H7422-40 and H7421-40, Hamamatsu) were used to detect SHG and autofluorescence, respectively.

The specimens were placed into a home-built chamber, which was specially tailored for LA-NOM to image the fresh tissue. A two-photon excitation laser light (wavelength of 760 nm) was used for LA-NOM imaging of the lung specimens. The excitation beam was focused and the emitted signals were collected through a low magnification apochromat objective (UPLSAPO $20 \times /0.75$ NA, Olympus) to achieve a large field of view and high spatial resolution. The lateral and axial resolution was 0.9 μm and 2.1 μm , respectively. The imaging area of each section was $\sim 2.2 \text{ mm} \times 2 \text{ mm}$ composed of 13×13 small area optical scanning images with $200 \text{ }\mu\text{m} \times 200 \text{ }\mu\text{m}$ (256×256 pixels). The dwell time per pixel was 24 μs and the time per small optical scanning image was 1.6 s. The axial image stacks were generated using a 2 μm step size. For each specimen, three image stacks were acquired at different regions. Six image stacks were obtained at each time point and a total of 60 image stacks were achieved in this study. To perform the quantitative comparison, all of the specimens were imaged

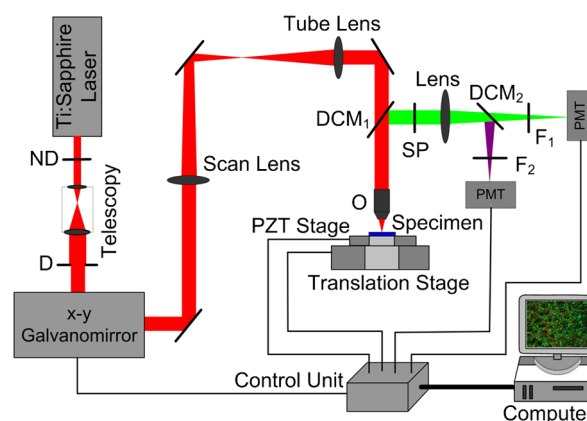


Fig. 1 Setup of large area nonlinear optical microscopy. ND: neutral density filter; D: diaphragm; DCM: dichroic mirror; SP: short-pass filter; F: band-pass filter; O: objective lens; PZT stage: piezoelectric stage; PMT: photomultiplier tube.

with the same average power of 7.8 mW. All imaging was completed within four hours after the animal sacrifice.

2.3 Quantification of MAF and SHG Images

2.3.1 MAFIR and SHGIR

To quantitatively analyze the variations of MAF and SHG intensity during the process of cancer cells colonization, MAFIR and SHGIR are employed in the study, defined as the ratio of MAF and SHG intensity in pathological tissue to that in normal tissue. The calculation steps of MAFIR are: First, the maximal MAF intensity value in all of the 60 MAF image stacks was chosen and used to normalize all the image stacks. Second, at each time point, the sum of MAF intensity in each image stack was calculated by adding the MAF intensity of all the pixels throughout the whole imaging volume. Then the average MAF intensity at each time point was obtained by the datum of six image stacks. At last, MAFIRs were calculated by the average MAF intensity of normal tissue and pathological tissue at different time points. Using the same method the SHGIR can be also calculated.

2.3.2 MAFSI

In order to eliminate the individual differences between the different mice as much as possible, MAFSI is used to quantify the relative intensity variation between cellular MAF and ECM SHG in tissue. For each two-dimension nonlinear optical image, MAFSI was calculated according to the formula $(P_{\text{MAF}} - P_{\text{SHG}})/(P_{\text{MAF}} + P_{\text{SHG}})$, in which P_{MAF} and P_{SHG} were the MAF and SHG intensity cumulated of all pixels in the same imaging section, respectively. As a result, the more MAFSI value approaching the maximum value of 1, the higher content level of the MAF presenting in the imaging section.

3 Results

3.1 Morphological Analysis

Large-area and high-resolution MAF, SHG and merged MAF and SHG images of normal C57BL/6 mice pulmonary tissue are shown in the first row of Fig. 2(a)–2(c). The imaging depth is 2 μm below the lung tissue surface. The magnified views of marked areas in Fig. 2(a)–2(c) are shown in

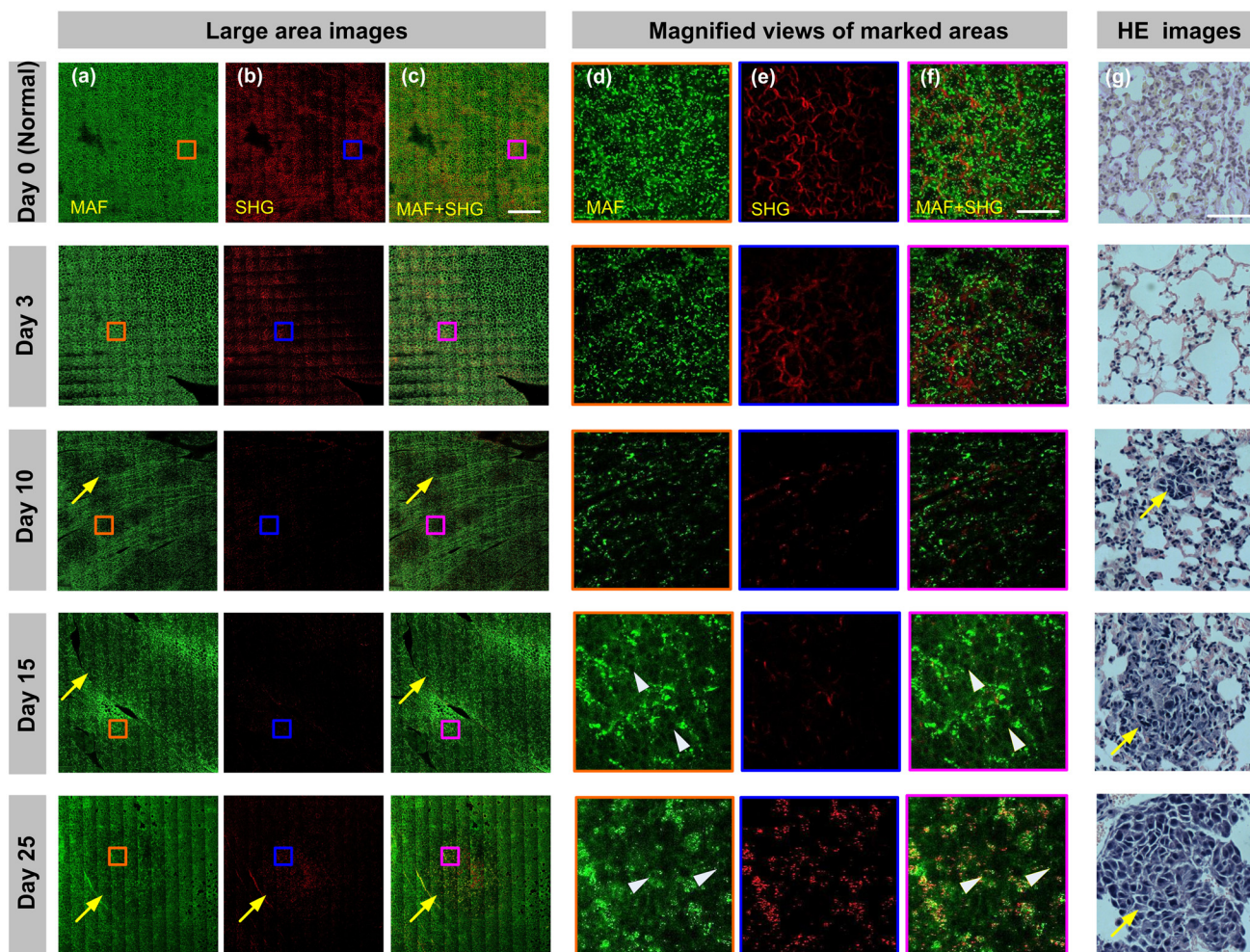


Fig. 2 MAF and SHG imaging for normal pulmonary tissue and pathological pulmonary tissue of C57BL/6 mice on the time of days 3, 10, 15, 25 after tail vein injection. (a)–(c) are MAF, SHG and merged MAF and SHG large area images (2.2 mm \times 2.2 mm). The arrows indicate the intact nodules. Scale bar is 400 μm . (d)–(f) are magnified views of marked areas in (a)–(c), respectively. The magnified MAF images reveal that the uniform structure of alveolus has been destroyed gradually and cancer cells appeared after day 15, while the continuous collagen have been ruptured into point-point distribution in the pulmonary metastasis nodules. The arrowheads show cancer cells. Scale bar is 40 μm . (g) HE images of pulmonary tissue at different time points. Scale bar is 40 μm .

Fig. 2(d)–2(f), respectively. Morphologically, observation from MAF images in the first row of Fig. 2(a) and 2(d) shows that alveoluses have uniform structure and are evenly distributed in the normal tissue. As illustrated in the first row of Fig. 2(b) and 2(c), collagen fibers are continuously distributed with high density in the normal tissue. In addition, image-merged MAF and SHG in the first row of Fig. 2(f) shows that the collagen fibers are round in the vicinity of the alveoli regularly in the normal tissue.

Unlike in the normal tissue, the morphologic features of pathological tissue become disorderly with the time-lapse after tail vein injection. The representative results of day 3, day 10, day 15, and day 25 are also shown in Fig. 2. As illustrated in Fig. 2, the feature of lung tissue at day 3 is similar with the normal tissue, except the low intensity of the MAF and SHG. After day 10, the small nodules appear in the lung tissue, while the profile of alveolus becomes blurry and the collagen fibers become discontinuous. Particularly after day 15, the cancer cells are clearly observed in the MAF image, as indicated by the arrowheads in Fig. 2. MAF and SHG images of intact nodules are shown by the arrows, especially at day 25, which reveals that the structures of alveolus are disappeared and the collagen fibers ruptured into point-point distribution in the pulmonary metastasis nodules.

In order to validate the MAF and SHG imaging, HE images at different time points are also shown in the Fig. 2. Compared with normal tissue, the alveolar units disrupt in early stage and disappear in the late stage. At day 10, the cancer cells can be easily distinguished from normal cells for their large and anomalous nuclei. With the time elapsed, the volume of cancer cell nuclei increase rapidly, especially in the late stage. At day 25, the cancer cell nuclei are much larger than the normal cell nuclei and take up the major space of tissue. In addition, the normal lung tissue is abundant in collagen fiber, while the metastasis tissues are rich in vessels and cancer cell nuclei.

3.2 Quantitative Analysis

The process of the pulmonary melanoma metastasis reflected by morphologic feature can also be quantified. The MAFIR and SHGIR of pathological pulmonary tissue and normal tissue are shown in the Fig. 3. Combined with Fig. 2, three stages are divided by the time points of nodules appearing in microscope and being macroscopical. As illustrated in Fig. 3, both of the MAF and SHG intensity decrease at early stage from day 0 to day 7. The MAF intensity increases in the middle stage from day 10 to day 15 and decreases again in late stage after day 15, while the SHG intensity reduces to and maintains in a certain level after day 10. The two-tailed student's *t*-test is performed on the MAFIR and SHGIR matrixs ($n = 6$) at different stages, as shown in Fig. 3. The MAFIRs have significant difference, while the SHGIRs cannot be distinguished between each other in each stage. Nevertheless, the results demonstrate that MAFIR provided by LA-NOM can succeed in monitoring the process of the metastasis.

Layer-resolved MAFSI as a function of depth for the specimens excised at different time points are shown in Fig. 4. The markers represent mean of MAFSI data and the curves are the fitting results. The results reveal that both the surface of normal tissue and pathological tissue are rich in collagen fibers and the density of the collagen fiber decreases with the depth in the tissue. The results of *t*-test shown in Fig. 4(a) reveal that MAFSI can be effectively employed to monitor the pathologic

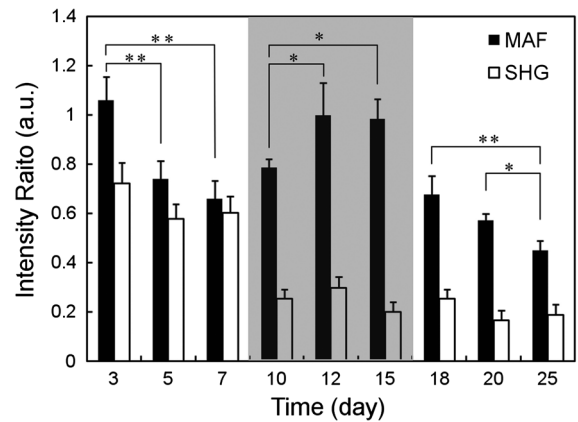


Fig. 3 MAFIR and SHGIR of pathological pulmonary tissue at different time points. All the MAF and SHG intensity in imaging volume of $2.2 \text{ mm} \times 2.2 \text{ mm} \times 30 \mu\text{m}$ at different time points were normalized according to the intensity of normal pulmonary tissue. $n = 6$; error bars indicate standard deviation; asterisk, $P < 0.05$ double asterisk, $P < 0.01$ calculated using a two-tailed student's *t*-test for the MAFIR and SHGIR in early (days 3, 5, and 7), middle (days 10, 12, and 15, marked by shadow rectangle) and late (days 18, 20, and 25) stages, respectively.

stages of lung tissue in early stage without nodules. However, in the middle stage (from day 10 to 15), the MAFSIs have no significant difference at any depth. After day 15, MAFSIs decrease in the tissue surface, but maintain a certain value at depth below $20 \mu\text{m}$. The MAFSIs have significant difference at depth of $0 \sim 8 \mu\text{m}$, which can be used to monitor the physiological changes of pulmonary melanoma metastasis in late stage.

4 Discussion

The process of cancer metastasis consists of a long series of sequential and interrelated steps: tumor cells detach from the primary tumor, intravasate into the blood vessels or lymphatics, circulate in the body, adhere to vessel wall of distant organs, extravasate vessels, establish a new microenvironment and proliferate at the new site.² It has been demonstrated that degradation of collagen in ECM can promote invasion and metastasis of cancer cells.²⁹ With the malignant melanoma cells metastasizing into lung tissue, the ECM will be remodeled resulting in the transformation of density and distribution of collagen fibers,^{18,23,30} which leads to the SHGIR decrease as shown in Fig. 3. The reduction of MAFIR from day 3 to day 7 in Fig. 3 may be induced by the decrease of the normal cells in the tissue, which is also revealed by the HE images from day 3 to day 7. At the middle stage, the proliferation of cancer cells and imposing metabolic stress of the tissue—which are enhanced by the remodeled tissue structure, growth factors released by tissue stroma and no pressure from the surrounding microenvironment—lead to the MAFRI rising from day 10 to day 15.^{9,31} Eventually, unconstrained proliferation of cancer cell without migration results in large nodules within a “capsule” of ECM, which can induce the cell apoptosis due to the limited availability of nutrients and oxygen.^{9,32} It has been demonstrated that excessive proliferative signaling can also trigger cell senescence and/or apoptosis.^{33–35} In addition, the large nucleus of the cancer cell colonizing in the lung tissue cannot provide MAF, which is another reason of MAFRI reduction in later staged after day 18. According to the definition of MAFSI, the inflection

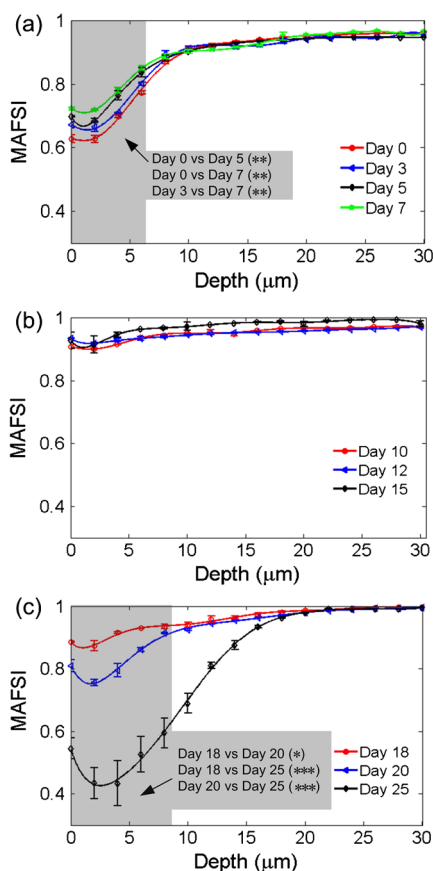


Fig. 4 Layer-resolved MAFSI as a function of depth in normal pulmonary tissue and pathological pulmonary tissue. A two-tailed student's t -test is performed on the MAFSI matrix ($n = 6$) at each depth point between different time points. (a)–(c) The MAFSI versus depth in early stage (days 0, 3, 5, and 7), middle stage (days 10, 12, and 15) and late stage (days 18, 20, and 25). The shadow rectangles in (a) and (c) indicate that the curves can be significantly distinguished by the P value of t -test at special depth in the tissue. Error bars indicate standard error of mean; asterisk, $P < 0.05$ double asterisk, $P < 0.01$ triple asterisk, $P < 0.001$.

point of each curve in Fig. 4 reveals that the density of collagen fibers at the depth of $\sim 2 \mu\text{m}$ is much higher than that at any other depth. In Fig. 4(a)–4(c), the changes of MAFSIs versus time, especially in the tissue surface, are primarily induced by the cooperation of MAF and SHG intensity discussed above.

In order to achieve large area images, the specimens were pressed lightly by a cover slip in the chamber. Our results reveal that this treatment has little influence on the morphologic features of lung tissue. Furthermore, quantitative parameters mentioned above can effectively eliminate this influence, mostly because MAFIR (SHGIR) is calculated using the MAF (SHG) intensity of the whole images stack and MAFSI represents the relative density of cellular chromophores and collagen fibers in each imaging section.

The imaging depth of NOM depends on the tissue properties of absorption and scattering, the excitation wavelength, the excitation laser power on the tissue, and the MAF and SHG signals-detection efficiency.³⁶ Generally, the imaging depth of NOM can be up to 100 micrometers in the fresh lung tissue.^{21,37} In our study, we used the excitation wavelength of 760 nm, which is the optimal excitation wavelength for NAD(P)H and FAD.³⁸ Non-descanned detection, the most efficient fluorescence

collection scheme,³⁹ and GaAsP photocathode PMT with high quantum efficiency ($\sim 42\%$ QE at peaking wavelength) used in the home-built system can provide high MAF and SHG signals-detection efficiency. Although, the detailed tissue structural information degrade with the increasing imaging depth, our home-built LA-NOM can allow for imaging depth of $\sim 120 \mu\text{m}$ in the lung tissue. However, the density of collagen fibers decreases with the depth and maintains a low level in deep lung tissue below $20 \mu\text{m}$. Therefore, the MAF and SHG images were only obtained up to $30 \mu\text{m}$ below the tissue surface in this study.

In the middle and late stage of cancer, the macroscopic nodules can be easily discriminated from the lung tissue and its number and volume also can reflect the process of cancer. However, there is no nodule in the early stage of cancer. The physiological changes of the tissue should be evaluated during the whole process of pulmonary melanoma metastasis, especially during the early stage of cancer.^{2,8,10} In addition, metastasis is a cell- and tissue-driven process, for which cancer cells and ECM interact and react throughout the progression of the disease.⁹ Therefore, monitoring the progress of pulmonary melanoma metastasis by label-free imaging with submicron spatial resolution is of significance.

For monitoring the process of metastasis, *in vivo* imaging that can eliminate the individual differences between the mice induced by the intrinsic properties of the tumor cells and responses of the host² can show more natural information than *ex vivo* imaging. Two techniques can achieve *in vivo* imaging with subcellular resolution; video-rate microscopy combined with a special window chamber and endoscopy.^{37,40–42} Nevertheless, to apply these new methods to diagnosis and therapy, understanding the process of metastasis at the cellular level by using conventional full-format microscope is absolutely a prerequisite. The pilot study is helpful for the future *in vivo* applications of those new methods, such as endoscopy.

5 Conclusion

In summary, we achieved label-free monitoring the progress of pulmonary melanoma metastasis of C57BL/6 mice *ex vivo* by LA-NOM. Microscopic morphologic changes during the process of pulmonary melanoma metastasis were depicted by MAF and SHG images at different time points. In addition, quantitative parameters, such as MAFRI, SHGRI, and MAFSI were used to quantify the pathological changes of pulmonary melanoma metastasis based on MAF and SHG intensity, especially in early and late stage after tail vein injection. Combining morphological analysis and quantitative analysis of the tissue, our results demonstrate that LA-NOM can be used to monitor the process of pulmonary melanoma metastasis, which indicates that LA-NOM can provide a powerful tool for the research in tumor pathophysiology and therapy evaluation.

Acknowledgments

This work was supported by National Major Scientific Research Program of China (No. 2011CB910401), National Natural Science Foundation of China (No. 61178077), Program for New Century Excellent Talents in University (No. NCET-08-0216) and Youth Science and Technology Program (No. 201271031424). The authors also thank the Analytical and Testing Center (Huazhong University of Science and Technology) for spectral measurements.

References

- D. S. Rigel, J. Russak, and R. Friedman, "The evolution of melanoma diagnosis: 25 years beyond the ABCDs," *CA Cancer J. Clin.* **60**(5), 301–316 (2010).
- I. J. Fidler, "Timeline—the pathogenesis of cancer metastasis: the 'seed and soil' hypothesis revisited," *Nat. Rev. Cancer* **3**(6), 453–458 (2003).
- J. H. Lee et al., "Biological factors, tumor growth kinetics, and survival after metastasectomy for pulmonary melanoma," *Ann. Surg. Oncol.* **16**(10), 2834–2839 (2009).
- E. S. Hwang et al., "In vivo tumor suppression activity by T cell-specific T-bet restoration," *Int. J. Cancer* **127**(9), 2129–2137 (2010).
- C. Martinez et al., "Experimental model of pulmonary metastasis treatment with IFN alpha," *Cancer Lett.* **225**(1), 75–83 (2005).
- H. Prydz et al., "Ex vivo and in vivo delivery of anti-tissue factor short interfering RNA inhibits mouse pulmonary metastasis of B16 melanoma cells," *Clin. Cancer Res.* **12**(13), 4055–4061 (2006).
- H. Z. Yang et al., "Blocking TLR2 activity attenuates pulmonary metastases of tumor," *PLoS One* **4**(8), e6520 (2009).
- C. L. Chaffer and R. A. Weinberg, "A perspective on cancer cell metastasis," *Science* **331**(6024), 1559–1564 (2011).
- P. Friedl and S. Alexander, "Cancer invasion and the microenvironment: plasticity and reciprocity," *Cell* **147**(5), 992–1009 (2011).
- N. Sethi and Y. Kang, "Unravelling the complexity of metastasis—molecular understanding and targeted therapies," *Nat. Rev. Cancer* **11**(10), 735–748 (2011).
- G. Kuttan and C. Manesh, "Effect of naturally occurring allyl and phenyl isothiocyanates in the inhibition of experimental pulmonary metastasis induced by B16F-10 melanoma cells," *Fitoterapia* **74**(4), 355–363 (2003).
- G. Kuttan and C. Guruvayoorappan, "Effect of amentoflavone on the inhibition of pulmonary metastasis induced by B16F-10 melanoma cells in C57BL/6 mice," *Integr. Cancer Ther.* **6**(2), 185–197 (2007).
- M. H. Frankel et al., "Isolation of tumorigenic circulating melanoma cells," *Biochem. Biophys. Res. Commun.* **402**(4), 711–717 (2010).
- Y. Fang et al., "Anticancer properties of 10-hydroxycamptothecin in a murine melanoma pulmonary metastasis model in vitro and in vivo," *Toxicol. In Vitro* **25**(2), 513–520 (2011).
- W. G. Seo et al., "Suppressive effect of Zedoariae rhizoma on pulmonary metastasis of B16 melanoma cells," *J. Ethnopharmacol.* **101**(1–3), 249–257 (2005).
- W. Denk, J. H. Strickler, and W. W. Webb, "Two-photon laser scanning fluorescence microscopy," *Science* **248**(4951), 73–76 (1990).
- W. W. Webb et al., "Live tissue intrinsic emission microscopy using multiphoton-excited native fluorescence and second harmonic generation," *Proc. Natl. Acad. Sci.* **100**(12), 7075–7080 (2003).
- N. D. Kirkpatrick, M. A. Brewer, and U. Utzinger, "Endogenous optical biomarkers of ovarian cancer evaluated with multiphoton microscopy," *Cancer Epidemiol. Biomarkers* **16**(10), 2048–2057 (2007).
- C. C. Wang et al., "Label-free discrimination of normal and pulmonary cancer tissues using multiphoton fluorescence ratiometric microscopy," *Appl. Phys. Lett.* **97**(4), 043706 (2010).
- L. M. Loew and P. J. Campagnola, "Second-harmonic imaging microscopy for visualizing biomolecular arrays in cells, tissues and organisms," *Nat. Biotechnol.* **21**(11), 1356–1360 (2003).
- M. C. Schanne-Klein et al., "Three-dimensional investigation and scoring of extracellular matrix remodeling during lung fibrosis using multiphoton microscopy," *Microsc. Res. Tech.* **70**(2), 162–170 (2007).
- M. B. Lilledahl et al., "Characterization of vulnerable plaques by multiphoton microscopy," *J. Biomed. Opt.* **12**(4), 044005 (2007).
- C. D. Davies et al., "Second-harmonic generation in collagen as a potential cancer diagnostic parameter," *J. Biomed. Opt.* **13**(5), 054050 (2008).
- X. Jian, S. Zhuo, and J. Chen, "Diagnostic application of multiphoton microscopy in epithelial tissues," *J. Innov. Opt. Health Sci.* **4**(2), 159–163 (2011).
- P. Wilder-Smith et al., "In vivo multiphoton fluorescence imaging: a novel approach to oral malignancy," *Laser Surg. Med.* **35**(2), 96–103 (2004).
- N. Ramanujam et al., "Multiphoton microscopy of endogenous fluorescence differentiates normal, precancerous, and cancerous squamous epithelial tissues," *Cancer Res.* **65**(4), 1180–1186 (2005).
- C. C. Wang et al., "Early development of cutaneous cancer revealed by intravital nonlinear optical microscopy," *Appl. Phys. Lett.* **97**(11), 113702 (2010).
- W. Zheng et al., "Diagnostic value of nonlinear optical signals from collagen matrix in the detection of epithelial precancer," *Opt. Lett.* **36**(18), 3620–3622 (2011).
- L. M. Matrisian and C. E. Brinckerhoff, "Timeline—matrix metalloproteinases: a tail of a frog that became a prince," *Nat. Rev. Mol. Cell Biol.* **3**(3), 207–214 (2002).
- F. Kheradmand, K. J. Greenlee, and Z. Werb, "Matrix metalloproteinases in lung: multiple, multifarious, and multifaceted," *Physiol. Rev.* **87**(1), 69–98 (2007).
- S. Alexander and P. Friedl, "Cancer invasion and resistance: interconnected processes of disease progression and therapy failure," *Trends Mol. Med.* **18**(1), 13–26 (2012).
- G. P. Gupta and J. Massague, "Cancer metastasis: building a framework," *Cell* **127**(4), 679–695 (2006).
- S. W. Lowe, E. Cepero, and G. Evan, "Intrinsic tumour suppression," *Nature* **432**(7015), 307–315 (2004).
- M. Collado and M. Serrano, "Senescence in tumours: evidence from mice and humans," *Nat. Rev. Cancer* **10**(1), 51–57 (2010).
- D. Hanahan and R. A. Weinberg, "Hallmarks of cancer: the next generation," *Cell* **144**(5), 646–674 (2011).
- A. K. Dunn et al., "Influence of optical properties on two-photon fluorescence imaging in turbid samples," *Appl. Opt.* **39**(7), 1194–1201 (2000).
- M. R. Looney et al., "Stabilized imaging of immune surveillance in the mouse lung," *Nat. Methods* **8**(1), 91–96 (2011).
- W. W. Webb, S. H. Huang, and A. A. Heikal, "Two-photon fluorescence spectroscopy and microscopy of NAD(P)H and flavoprotein," *Biophys. J.* **82**(5), 2811–2825 (2002).
- W. R. Zipfel, R. M. Williams, and W. W. Webb, "Nonlinear magic: multiphoton microscopy in the biosciences," *Nat. Biotechnol.* **21**(11), 1368–1376 (2003).
- L. Fu et al., "Nonlinear optical endoscopy based on a double-clad photonic crystal fiber and a MEMS mirror," *Opt. Express* **14**(3), 1027–1032 (2006).
- Y. Liu et al., "Visualization of hepatobiliary excretory function by intravital multiphoton microscopy," *J. Biomed. Opt.* **12**(1), 014014 (2007).
- X. D. Li et al., "Scanning all-fiber-optic endomicroscopy system for 3D nonlinear optical imaging of biological tissues," *Opt. Express* **17**(10), 7907–7915 (2009).